Nanosecond Laser Ablation of Au@LiNbO$_3$ Core–Shell Nanoparticles in Ethanol: Properties and Application in Optoelectronic Devices

Raid A. Ismail[1] · Evan T. Salim[1] · Marwa S. Alwazny[1,2]

Abstract

Core/shell nanocomposite is a very interesting structure that exhibits excellent properties such as improved thermal stability and decreased reactivity of the core nanoparticles. Core/shell nanoparticles were synthesized by means of laser ablation in ethanol without using a catalyst. The structural and optical properties of Au@LiNbO3 core/shell nanoparticles as a function of laser fluence are investigated. To fabricate the photodetector, a thin film of Au@LiNbO$_3$ was deposited on a single crystal silicon substrate. X-ray diffraction (XRD) results show that the synthesized nanocomposite is crystalline with a rhombohedral structure and the presence of peaks related to a gold cubic structure, indicating the formation of a core/shell nanocomposite. Transmission electron microscopy (TEM) investigations confirm the formation of core/shell spherical nanoparticles, whose size depends on the laser fluence. The optical properties reveal that the optical energy gap of LiNbO$_3$ was 4.08 eV, while the energy gap of the Au@LiNbO$_3$ core/shell prepared at 1.3, 1.6, 2, and 2.2 J/cm^2 was 3.6, 3.49, 3.4, and 3.8 eV, respectively. The optoelectronic properties of the Au@LiNbO$_3$/Si photodetector fabricated without a buffer layer and an antireflection coating as a function of laser fluence are investigated. The optoelectronic properties show that the maximum responsivity was 0.43 A/W at 400 nm for the Au@LiNbO$_3$/Si photodetector fabricated at 2 J/cm^2. The variation of laser fluence affects the structural, optical, and electrical properties of Au@LiNbO$_3$ core/shell. The best core/shell characteristics and photodetector were obtained at a laser energy of 2 J/cm^2. The energy band diagram confirmed that the presence of Au significantly improved the photoresponse of the photodetector.

Keywords Lithium niobate · Gold · Nanoparticles · Core/shell, Surface plasmon resonance · Laser fluence · Nanocomposite

Introduction

Because of its outstanding physicochemical, ferroelectric, piezoelectric, and nonlinear optical capabilities, lithium niobate is one of the interesting and promising ferroelectric materials [1–3]. Due to these properties, it has been widely applied in a variety of fields, including optical waveguides, electro-optical modulation, holographic storage, optical parametric oscillators, etc. [4, 5]. It belongs to the space group R3c and has rhombohedral symmetry. LN's ferroelectric phase changed to a paraelectric phase at 1200 °C. Due to its exceptional qualities, LiNbO3 has been widely used as a promising contender for "optical silicon." Nevertheless, LN serves as a passive component and an insulator in the aforementioned applications [6–8]. Many of the remarkable features of LN can be utilized in semiconductor integrated devices if LN devices can be integrated onto a silicon substrate to produce an active component, combining the advantages of both LN and semiconductor materials [9–11]. The main challenges in fabricating an active component based on the p–n junction were the low electrical conductivity and optical absorption of LN. In an attempt to fabricate a device using LN, it is necessary to increase the electrical conductivity of LN [12–14]. As reported, various methods were employed to synthesize LiNbO$_3$, for example, solution phase, sol–gel, citrate gel, electrospinning, and pulsed laser deposition [15–18]. There are many routes used to control the optical and electrical properties of LN, such as doping with different elements, for example Mg, Zn, Fe, etc. [19–22]. Several attempts to synthesize lithium niobate with a gold and silver core/shell structure have been reported.

✉ Raid A. Ismail
  raidismail@yahoo.com

1 Applied Science Department, University of Technology-Iraq, Baghdad, Iraq

2 Laser and Optoelectronic Department, University of Technology-Iraq, Baghdad, Iraq

Murillo et al. [2] deposited Ag–LiNbO$_3$ nanocomposite thin films with Ag nanoparticles (NPs) embedded into the LN matrix by the co-deposition of Ag and LN using a pulsed laser deposition (PLD) method that shows a surface plasmon resonance (SPR) in the visible range. The fabrication and characterization of a Fe-doped LiNbO$_3$/n-Si heterojunction was demonstrated by Li et al. [23]. As reported, on solid surfaces, gold nanoparticles were assembled into 2D or 3D superlattices, nanowires, colloidal aggregates, and a core/shell in order to improve their physical and chemical properties and enable them to be efficient for many important applications such as catalysts, sensors, photonics, and surface-enhanced Raman scattering [24–30]. Compared to other techniques, the laser ablation of Au@LiNbO$_3$ core/shell nanoparticles in liquid method used is promising and has several advantages including simplicity, low-cost, high purity product, fast, green synthesis, and fair control of the core–shell dimensions. [31–33]. The core–shell morphology give better thermal stability and decreases the reactivity.

Herein, we have demonstrated the synthesis of Au@LiNbO$_3$ core/shell nanoparticles by two- step laser ablation in methanol at different laser fluences. The fabrication of Au@LiNbO$_3$/Si was proposed as a simple, novel, and high-performance photodetector can used for many technological applications.

Experimental Work

Preparation of Au@LiNbO$_3$ Core–Shell Nanoparticles

Colloidal Au nanoparticles are prepared by irradiating a high purity (99.9%) Au pellet immersed in a vessel filled with 3 ml of ethanol with 70 laser pulses of a second harmonic generation (= 532 nm) Q-switched Nd:YAG laser with a pulse duration of 7 ns and a repetition frequency of 1 Hz to synthesize Au@LiNbO$_3$ core/shell nanoparticles. The ablation of Au nanoparticles was carried out at a laser fluence of 1.5 J/cm^2. After Au colloidal preparation, a LiNbO$_3$ wafer with an area of 1 cm^2 was placed in the quartz vessel filled with Au colloid and then irradiated with 300 laser pulses at a laser fluence of 1.3, 1.6, 2, and 2.2 J/cm^2. The experimental setup of the PLAL system is shown in Fig. 1a.

Characterization of Au @ LiNbO$_3$ Core/Shell Nanoparticles

The optical absorption of colloidal Au nanoparticles, LN nanoparticles, and Au@LiNbO$_3$ core/shell nanoparticles were measured using a UV–Vis spectrophotometer (Shimadzu UV-2550). The structural properties of the Au@LiNbO$_3$ core/shell were investigated using an X-ray diffractometer (Panalytical X'Pert Pro). A confocal Raman spectrometer was used to record Raman spectra (HORIBA XPLORA PLUS). Transmission electron microscopy (ZEISS LEO 912) was used to examine the morphology and size of the Au@LiNbO$_3$ core–shell.

Fabrication and Characterization of Au@LiNbO$_3$/Si Photodetector

Fabrication of Au@LiNbO$_3$/p-Si heterojunction photodetector was performed by depositing a thin-film Au@LiNbO$_3$ core/shell via a spin coating route on polished (111)-oriented p-type silicon substrate. The silicon substrates used here have areas of 1 cm^2 and electrical resistivity of 1–3 Ωcm. The ohmic contacts were made by the depositing of Al and In electrodes on the Au@LiNbO$_3$ nanostructure film and silicon substrate, respectively, by using the thermal resistive technique through a metal mask. Figure 1b shows the fabrication steps of the Au@LiNbO$_3$/Si photodetector. The current–voltage characteristics

Fig. 1 a Schematic diagram of detailed formation mechanism of Au @ LiNbO$_3$ core/shell nanoparticles by pulsed laser ablation in ethanol b Fabrication steps of Au@LN/Si photodetector
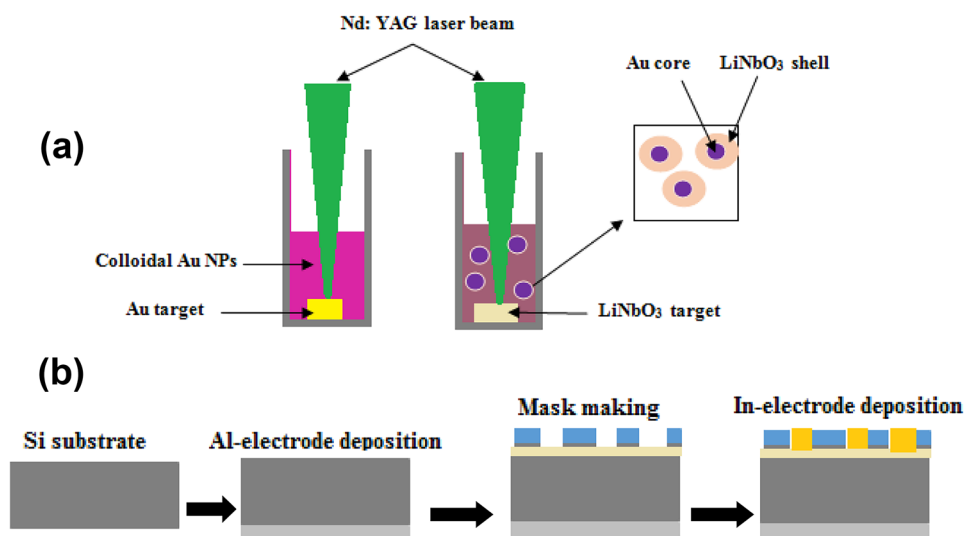
of the heterojunctions in the dark and under illumination were measured. The capacitance–voltage characteristics of the heterojunction were measured at a frequency of 200 kHz using LCR meter. The responsivity of the photodetector was measured using a monochromator (Jobin Yovn) in the spectral range of 370–1000 nm at a bias voltage of -8 V. The power calibration of the monochromator was performed using a silicon power meter.

Results and Discussion

Figure 2 shows the XRD pattern of Au@LN core/shell nanoparticles prepared at 1.3 J/cm^2, which exhibits two peaks located at $2\theta = 33.05°$ and $61.6°$ which correspond to the (104) and (214) planes, respectively. The XRD pattern of the nanoparticles prepared at 1.6 J/cm^2 shows the presence of eight XRD peaks located at $2\theta = 33.03°$, $35.9°$, 41.08, $47.7°$, $54.6°$, $56.3°$, $57.3°$, and $61.7°$, which correspond to (104), (110), (113), (024), (116), (122), (214), and (220) planes, respectively. While the XRD patterns of the core/shell synthesized at 2 J/cm^2 have six diffraction angles at $2 = 33.04°$, $35.84°$, $47.7°$, $54.5°$, $56.6°$, $57.3°$, and $61.7°$, corresponding to planes (104), (110), (024), (116), (122), and (214), respectively. Finally, the nanoparticles synthesized at 2.2 J/cm^2 show the presence of six diffraction peaks observed at $2\theta = 33.06°$, $35.9°$, $47.8°$, $54.6°$, $56.4°$, $57.3°$, and $61.7°$ corresponding to (104), (110), (024), (116), (122), and (214) planes, respectively. All the observed XRD peaks are indexed to a rhombohedral LiNbO$_3$ according to JCPDs#20-0631 [34–36]. The XRD peaks of core Au nanoparticles were observed at $2\theta = 44°$ and $66°$ which correspond to (200) and (220) planes, respectively.

Figure 3 depicts the UV–Vis absorption spectra of colloidal Au@LN core and shell prepared at various laser fluences. The optical absorption spectra display a general increase with increased laser fluence, besides two groups of absorption peaks, the first one is attributed to LiNbO$_3$ that is located at 224, 226, 227, and 231 nm for nanoparticles synthesized at 1.3, 1.6, 2, and 2.2 J/cm^2 laser fluence, respectively, with the shoulder diminishing at higher laser fluence. The second peak is located at ~ 521–530 nm, which belongs to the surface plasmon resonance (SPR) of the gold nanoparticles. This peak disappeared at laser fluence of 2.2 J/cm^2 This may be due to an increase in shell thickness. Increasing the LN shell thickness leads to decreasing the intensity of SPR of the Au core [37, 38]. The increase in LN concentration at higher laser fluence may be attributed to the low dipole moment of ethanol (1.69D) supporting growth via introducing extra species during the ablation, which results in a wider particle size distribution [39, 40]. Figure 4 displays the optical absorption of Au nanoparticles and the change in optical absorbance of LN nanoparticles after making the core/shell structure with Au nanoparticles.

The optical energy gap of LiNbO$_3$ and Au@ LiNbO$_3$ core/shell nanoparticles was estimated using Tauc's relationship [41–43]. The optical energy gap value is estimated by plotting $(\alpha h\nu)^2$ as a function of $h\nu$, and the extrapolation of the second region of the curve to the photon energy axis gives the energy gap, as shown in Fig. 5. The energy gaps of the Au@LN core–shell prepared at laser fluence of 1.3, 1.6, 2, and 2.2 J/cm^2 were 3.6, 3.49, 3.4, and 3.8 eV, respectively. The energy gap of LiNbO$_3$ was 4.12 eV, which is larger than that of the Au@LiNbO$_3$ core/shell structure. This could be attributed to the increased particle size of Au@LN due to the

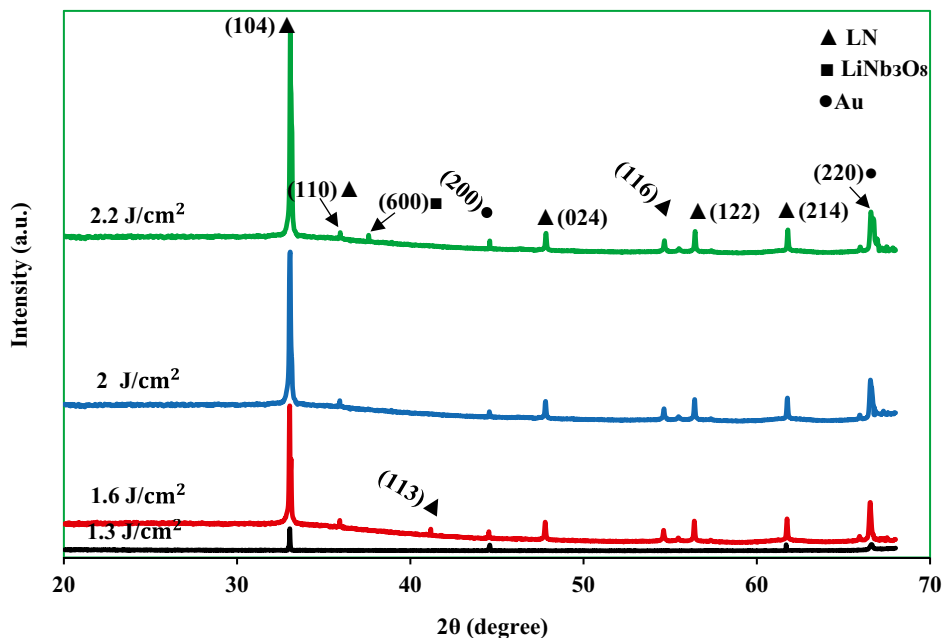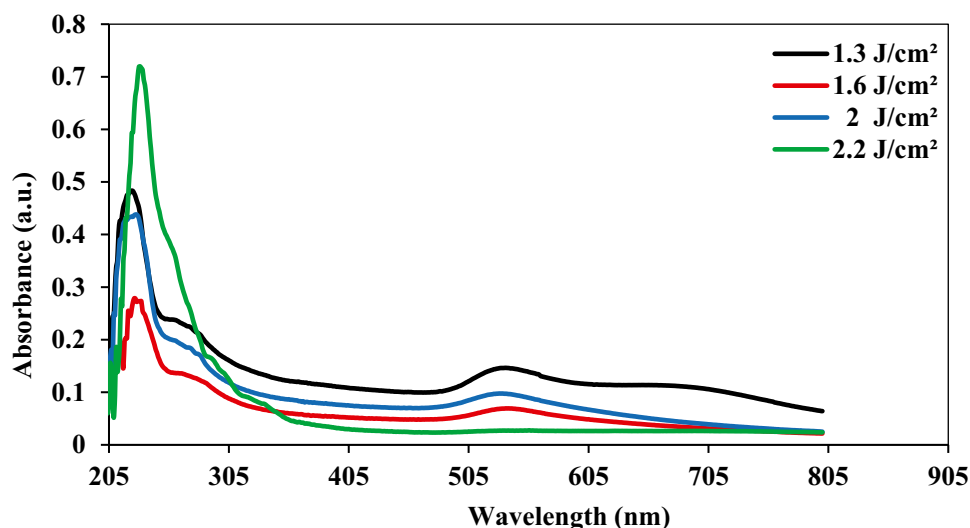**Fig. 2** XRD patterns of Au@ LN core/shell nanoparticles synthesized different laser fluences

Fig. 3 UV–Vis absorbance of Au/LiNbO$_3$ ablated in ethanol at different laser fluence

presence of the core–shell structure, as shown in Fig. 6. On the other hand, increasing the energy gap with laser fluence is due to the decrease in core–shell particle size.

The TEM images of Au@LN core/shell nanoparticles prepared at various laser fluences are shown in Fig. 7. These images confirm the formation of spherical nanoparticles with core/shell morphology, since the Au core nanoparticle is surrounded by a LN shell and the size of the core–shell particle depends on the laser fluence. The particle size increases first from 15 to 23 nm as laser fluence increases from 1.3 to 1.6 J/cm^2 and then decreases to 19 nm as laser fluence increases to 2.2 J/cm^2, and it shows a wide range of particle distribution. This gives approval to the change in shift of the absorption edge and the change in energy gap value of the UV–Vis results. Figure 8 shows the magnified TEM images of the core/shell structure, which revealed the formation of a monodispersed core/shell with

a very clear boundary between Au-core and LN-shell. The effect of laser fluence on the core size and shell thickness is shown in Fig. 9. As laser fluence increases, the core size and shell thickness increase up to the laser fluence of 2 J/cm^2 and further increases in laser fluence result in decreasing the core size and shell thickness due to fragmentation process.

Figure 10 shows the SEM images of Au@LiNbO$_3$ core/shell nanoparticles prepared at different laser fluences. These images reveal the formation of spherical nanoparticles and many, agglomerated and aggregated nanoparticles are observed.

Figure 11 shows the Raman spectra of Au@LiNbO$_3$ core–shell nanoparticles recorded in the range of 95–1000 cm^{-1}. For all samples except the one prepared at 1.6 J/cm^2, Fig. 10 confirms the presence of seven E modes and one A Raman mode indexed as E(TO), E4, E(6TO), E(LO6), E(LO7), (E-TO8), 4A1TO, and E(LO9). This result

Fig. 4 UV–Vis absorbance of Au@LiNbO$_3$, colloidal Au nanoparticles, and LiNbO$_3$ nanoparticles
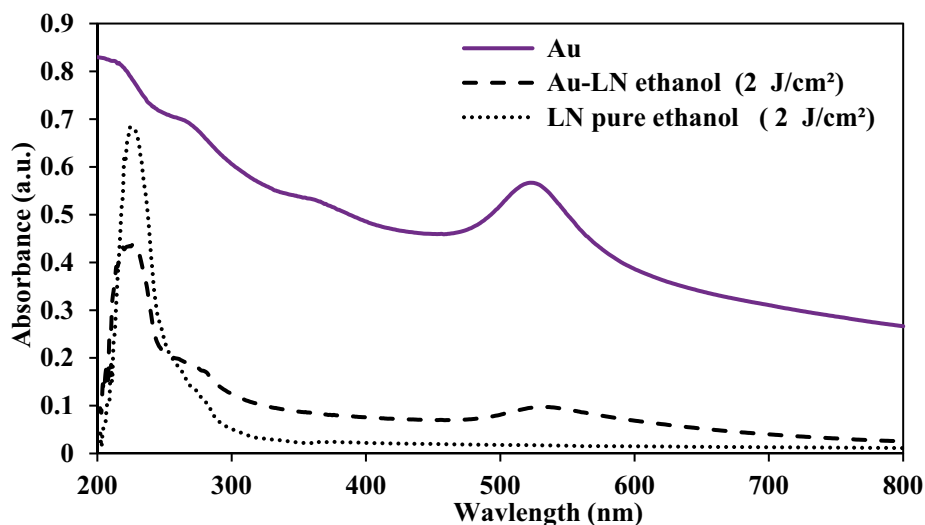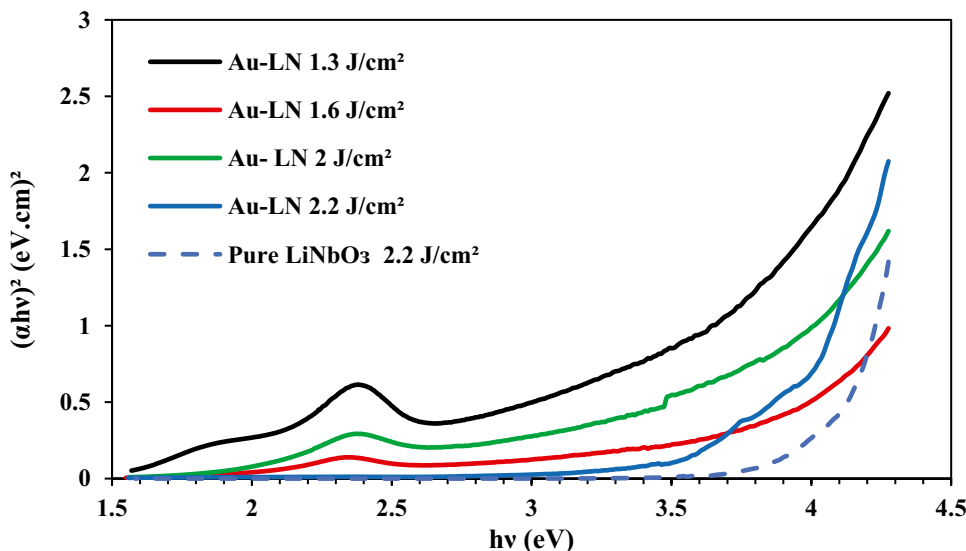
Fig. 5 $(\alpha h\nu)^2$ versus photon energy plot of LN and Au@LiNbO$_3$ prepared at different laser fluences


emphasizes that all observed phonon modes in Raman spectra for synthesized samples are consistent with the vibration modes for LiNbO$_3$ single crystal reported by other workers [44, 45]. As laser fluence increased, the peak intensity increases due to increasing the concentration of the core–shell nanoparticles. A significant enhancement in the Raman intensity may be produced after employing Au nanoparticles to LN structures due to the presence of plasmonic Au NPs, which play an essential role in the enhancement of the intensity of Raman peaks. This can originate from the local fields associated with the excitation of surface plasmon resonances by the Raman source [46, 47]. The vibration modes of the Au@LiNbO$_3$ core/shell samples as a function of laser fluence are listed in Table 1.

Figure 12 presents the zeta potential plots of the Au@LiNbO$_3$ core/shell synthesized at various laser fluences. The value of the zeta potential gives an indication of the potential stability of the colloidal Au@LiNbO$_3$ core/shell. As shown in Table 2, the best value of ZP was 32 mV for the sample prepared at a laser fluence of 2.2 J/cm^2, which indicates that colloidal suspensions are stable and no agglomeration and/or aggregation can be obtained. The origin of particle agglomeration is the van der Waals force and high surface energy. The nanoparticles synthesized at 2.2 J/cm^2 have the highest value of ZP due to their high concentration. Ions are adsorbed on the surface of the particles, affecting the value of the isoelectric point and, as a result, increasing particle dispersion.

Figure 13 illustrates the dark forward and reverse current–voltage characteristics of p-Au@LiNbO$_3$ NPs/p-Si heterojunction at room temperature. It is clearly seen that the samples exhibited rectifying properties, indicating the

Fig. 6 Particle size and energy gap of Au@LN core/shell as a function of laser fluence
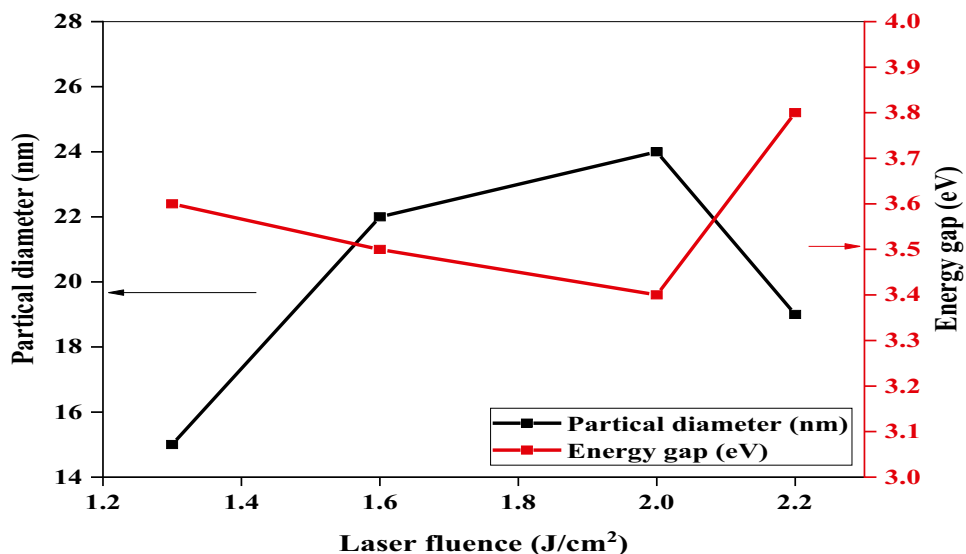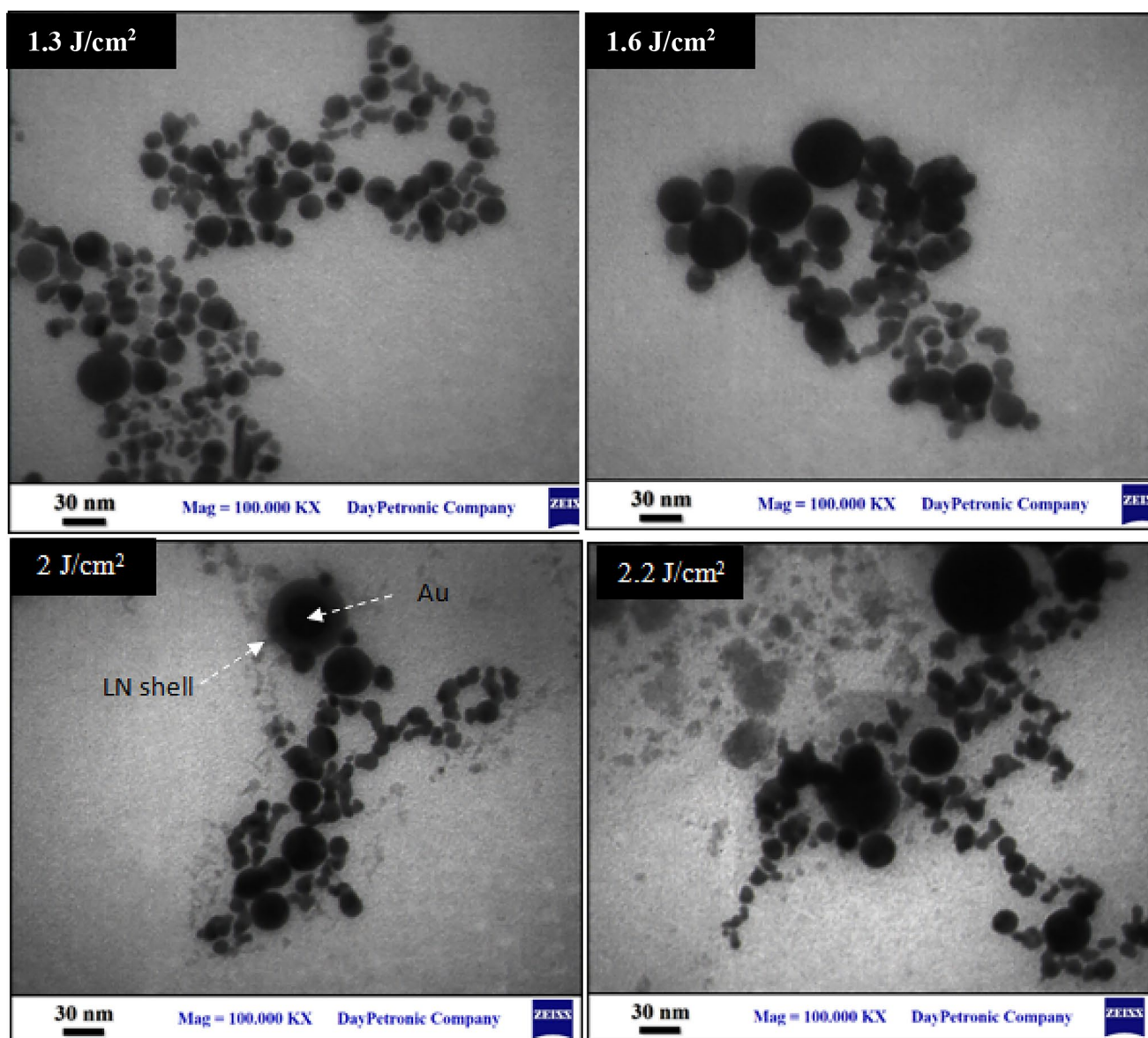
Fig. 7 TEM images of Au@LN core/shell nanoparticles synthesized at various laser fluences

formation of diode-like devices. The highest rectification factor was found for heterojunction prepared at 2 J/cm^2. As is obvious, the forward current increases as the bias voltage increases due to decreasing the depletion region, and the turn-on voltage was found to depend on the laser fluence. For heterojunctions prepared at 1.3 J/cm^2 and 1.6 J/cm^2, the turn-on voltage is less than 2 V, while it is greater than 2 V for samples prepared at 2 and 2.2 J/cm^2. This can be justified as a result of decreasing the electrical resistivity of the Au@LiNbO$_3$ core–shell as well as the dominance of diffusion current. The reverse current increases slightly for all samples with increasing bias voltage, particularly at voltages greater than 2 V. The forward current of the heterojunction prepared at 2 and 2.2 J/cm^2 is larger than the other fabricated heterojunctions due to the decreasing of the electrical resistivity of the nanoparticles.

The ideality factor β of the heterojunction could be extracted from diode equation [50]

$$I = I_s e^{\frac{qV}{\beta KT}} \tag{1}$$

where K is the Boltzmann constant, q is the electron charge, and I_s is the saturation current. The saturation current was determined from the Ln (I_f) versus V_f plot, where I_f is the forward current and V_f is the voltage at forward bias as shown in Fig. 14.

Fig. 8 Magnified TEM images of Au@LiNbO$_3$ core–shell nanoparticles synthesized at **a** 1.3, **b** 1.6, **c** 2, and **d** 2.2/cm^2
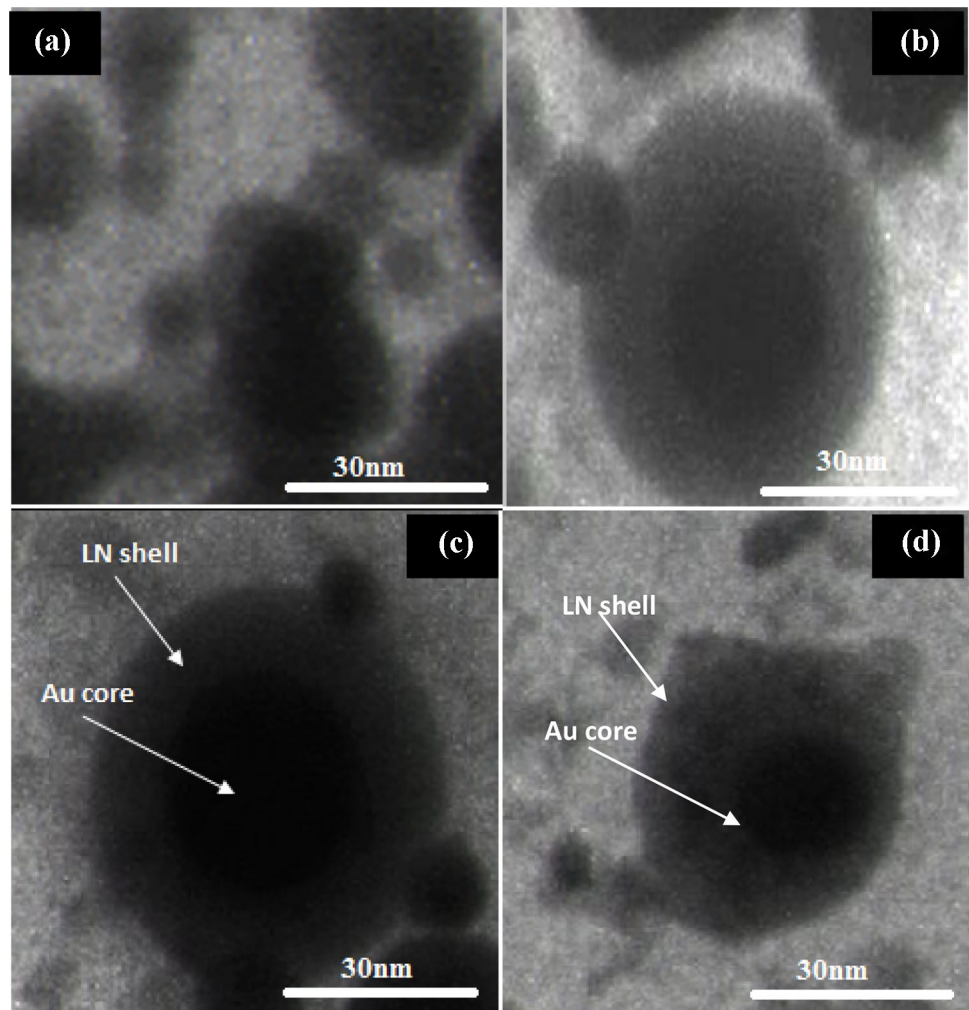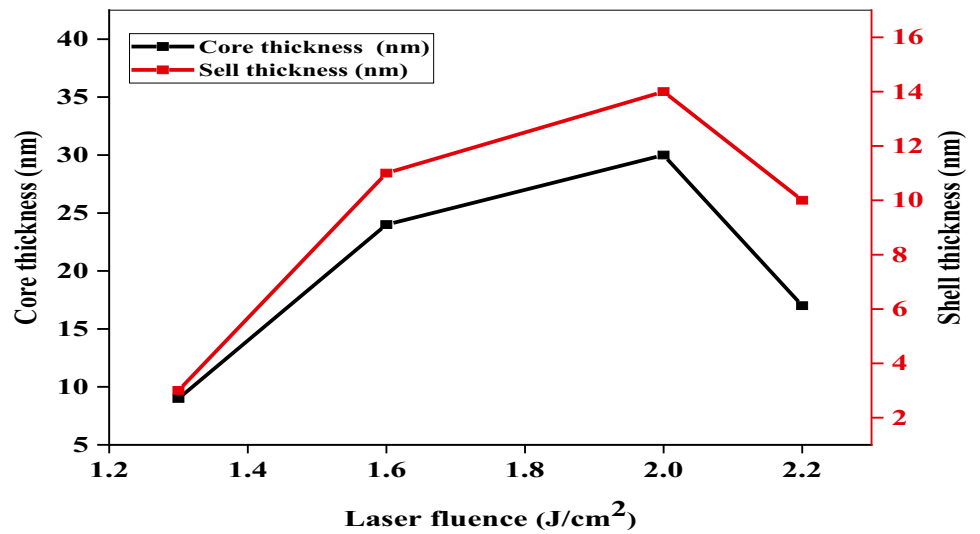

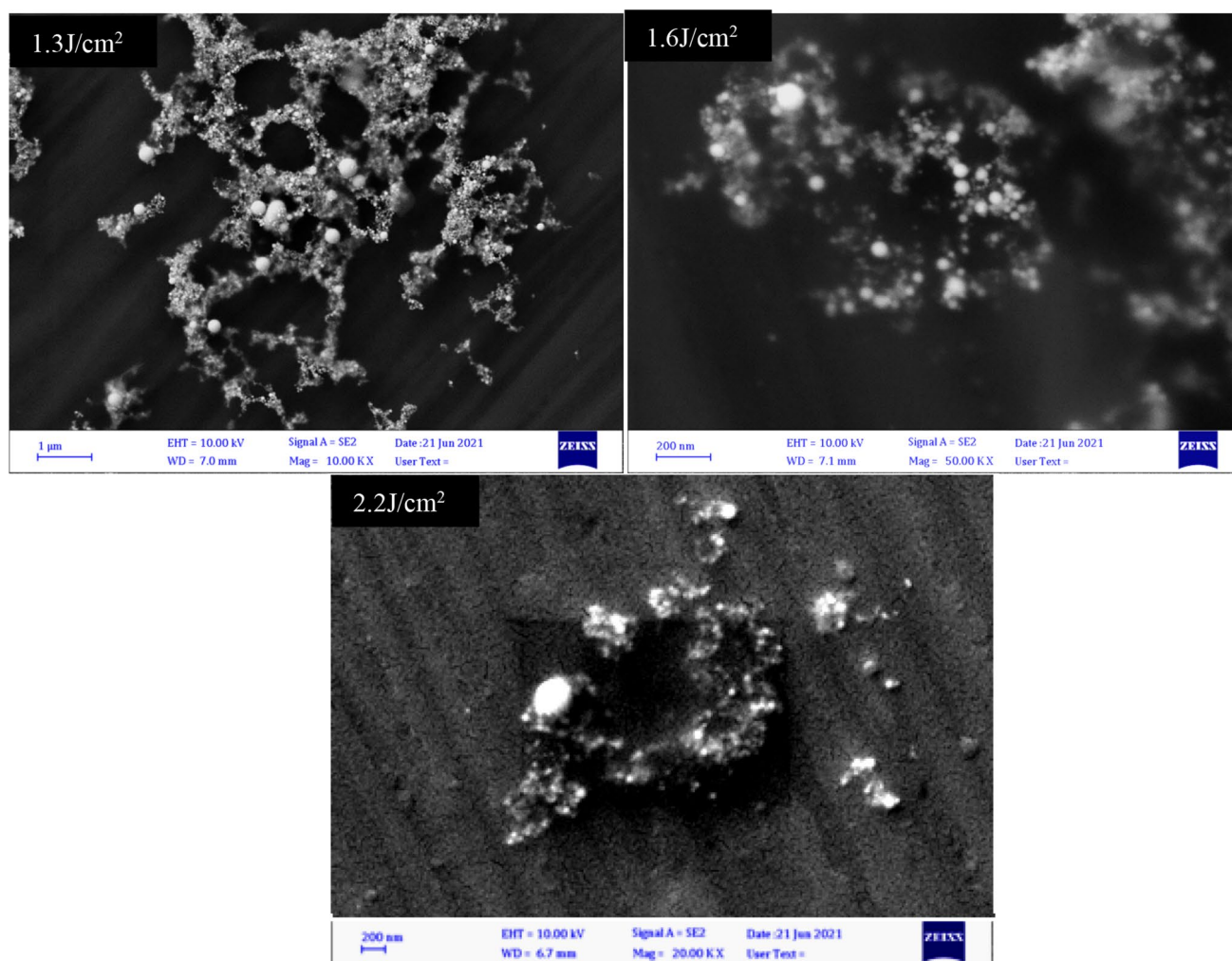**Fig. 9** Relationship between core size and shell thickness with laser fluence

Fig. 10 SEM images of core/shell prepared at various laser fluences

The ideality factors of the p-Au@LiNbO$_3$/p-Si hetero-junction devices fabricated at laser fluences of 1.3, 1.6, 2, and 2.2 J/cm^2 were 6.5, 3.9, 2.0, and 5.3, respectively. The large value of the ideality factor of the heterojunction indicates deviation from the ideal diode, suggesting the presence of defects like trapping, series resistance, and surface states arising from agglomeration and aggregation of the nanoparticles [51, 52]. The value of the ideality factor indicates that the heterojunction prepared at 2 J/cm^2 has the best junction characteristics. By using thermionic emission of current–voltage characteristics of the Au@LN/Si heterojunction, the barrier height Φ can be given by [53]:

$$\Phi = \frac{KT}{q} Ln \frac{AA^*T^2}{I_s} \tag{2}$$

where A is the area of the heterojunction and A^* is the Richardson constant. The values of the barrier height of the Au@LN NPs/Si heterojunctions fabricated at laser fluences of 1.3, 1.6, 2, and 2.2 J/cm^2 were 0.84, 0.83, 0.85, and 0.82 eV, respectively. The

capacitance voltage (C-V) characteristics of the heterojunctions are depicted in Fig. 15. The linear relationship indicates that the fabricated hetero-junctions are abrupt in nature. The value of the built-in-potential Vbi can be calculated by extrapolating the linear part to C^{-2}=0. The values of the built-in potential were 0.6, 0.5, 0.4, and 0.8 V for the heterojunctions prepared at 1.3, 1.6, 2, and 2.2/cm^2, respectively. As shown in Fig. 15, the capacitance of all heterojunctions is inversely proportional to the reverse bias voltage. The reduction in the device capacitance with bias voltage resulted from the widening of the depletion layer [54]. This properly gives an indication of the behavior of the charge transition between the junction sides [55]. Increasing the capacitance of the junction with laser fluence can be attributed to increasing the hole concentration of the core–shell nanoparticles. The linearity characteristics of the photodetectors are shown in Fig. 16. The photocurrent is plotted versus light intensity. This figure gives information about the linear dynamic range (LDR). The LDR is given by the following equation:

Fig. 11 Raman spectra of Au@ LiNbO$_3$ synthesized at various laser fluences
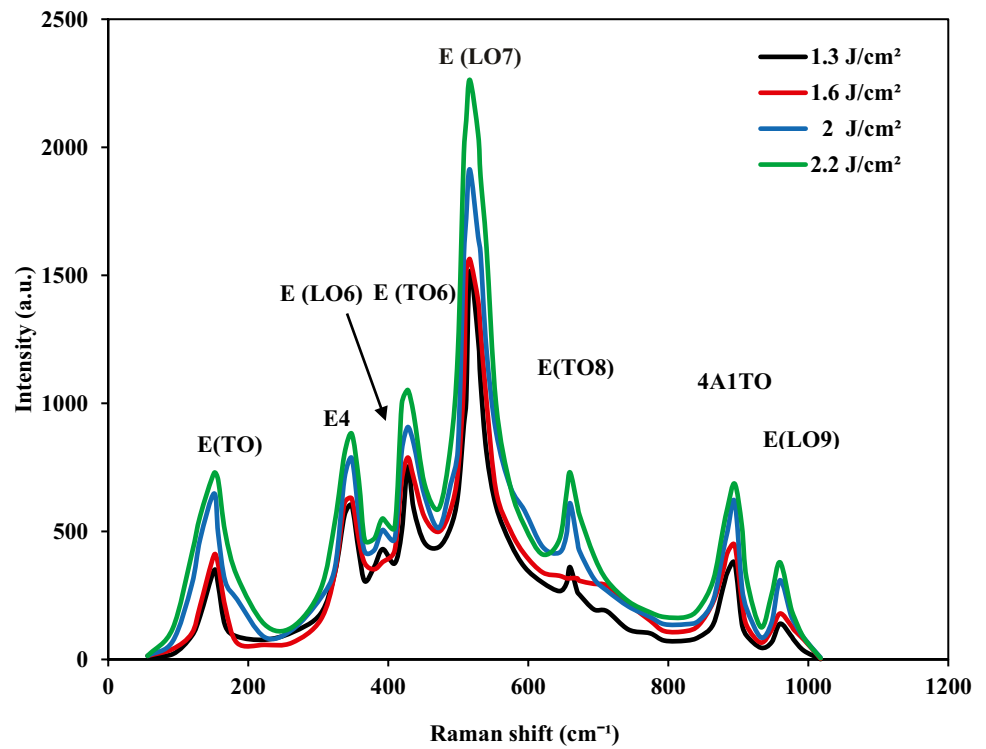
$$LDR = 20Log\frac{P_{max}}{NEP} \qquad (3)$$

where P$_{max}$ is the maximum amount of light that illuminated the photodetector and NEP is the noise equivalent power. The values of LDR estimated from Fig. 16 of the fabricated photodetector fabricated at 1.6, 2, and 2.2 J/cm^2 were 59, 152, and 61 dB, respectively.

Figure 17 shows the effect of laser fluence on the spectral responsivity R$_\lambda$ of the p-Au@LiNbO$_3$/p-Si photodetectors measured at reverse bias of − 8 V. A clear peak of response was observed at 399 nm for all heterojunctions, which can be indexed to the absorption edge of the Au@LiNbO$_3$ core–shell and a second peak appeared at 850 nm which attributed to the silicon substrate [56][57]. The maximum responsivity was 0.43 A/W at 400 nm for

Table 1 Raman vibration modes of Au @LiNbO$_3$ core/shell nanoparticles

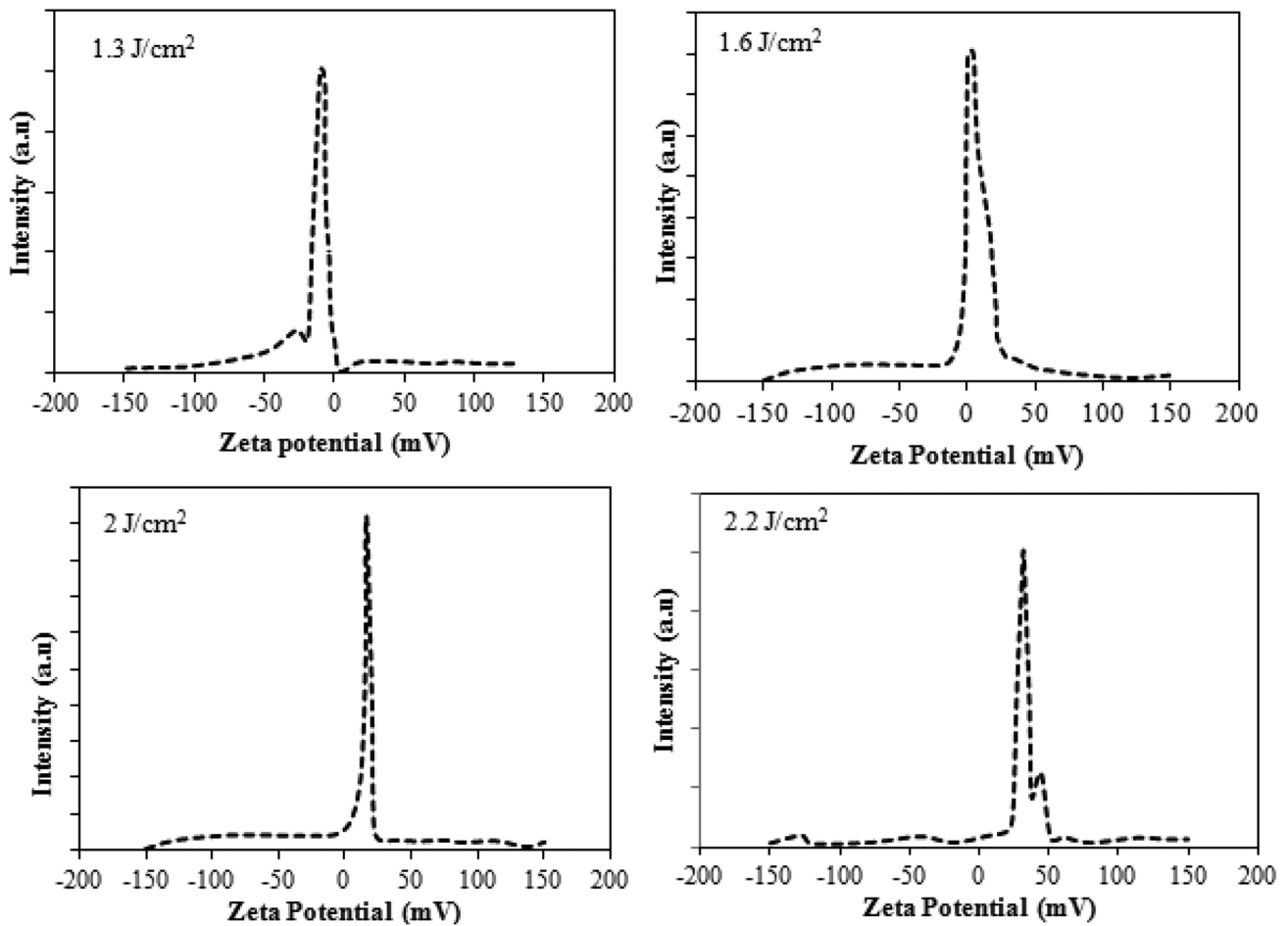| Modes	Reported LiNbO$_3$	Ref	Au@LiNbO$_3$			
			1.3 J/cm^2	1.6 J/cm^2	2 J/cm^2	2.2 J/cm^2
E(TO)	150	[48]	151	151	151	151
E4	340	[6]	347	347	347	347
E(6TO)	384	[6]	392	-	392	392
E(LO6)	424	[49]	427	427	427	427
E(LO7)	525	[49]	516	516	516	516
(E-TO8)	578	[46, 47]	569	-	569	569
4A1TO	890	[44, 45]	894	894	894	894
E(LO9)	988	[49]	959	959	959	959

Fig. 12 Zeta potential plots of Au@LiNbO$_3$ core/shell nanoparticles

the photodetector fabricated with 2 J/cm^2. Furthermore, a small peak appeared at 600 nm for the photodetector fabricated, which may be attributed to the SPR effect of the Au core. It is clearly noticed that It is clear that the photodetector's responsivity is dependent on laser fluence, which can be attributed to the increasing shell thickness with laser fluence. Increasing the shell thickness improves the responsiveness in the visible region. On the other hand,

an increase in the electrical resistivity of the nanoparticles leads to an extension of the depletion region toward the Au@LiNbO$_3$ and, in turn, enhances the short wavelength responsivity. The specific detectivity of the photodetector was calculated from the following equation:

$$D^* = \frac{A^{0.5}I_{ph}}{P\sqrt{2eI_d}} \tag{4}$$

where *A* is the sensitive area of the photodetector, *P* is the light power, *e* is the electron charge, *Id* is the dark current of the photodetector, and I*ph* is the photocurrent of the photodetector. The specific detectivity *D** of the photodetectors was determined as a function of laser fluence, as shown in Fig. 18. The maximum *D** was 1.32×10^{12} and 1.08×10^{12} Jones at 380 nm and 850 nm, respectively, for Au @ Au@ LN/p-Si photodetector fabricated at 2 J/cm^2. The presence

Table 2 ZP value as a function of laser fluence of Au @LiNbO$_3$ core/shell nanoparticles

Laser fluence (J/cm^2)	Zeta potential (mV)
1.3	− 8
1.6	2.9
2	16.15
2.2	32.32

Fig. 13 Effect of laser fluence on the dark forward and reversed current of p-Au@LiNbO$_3$/p-Si devices. Inset is the schematic illustration of Au@LiNbO$_3$/Si heterojunction with electrical configuration
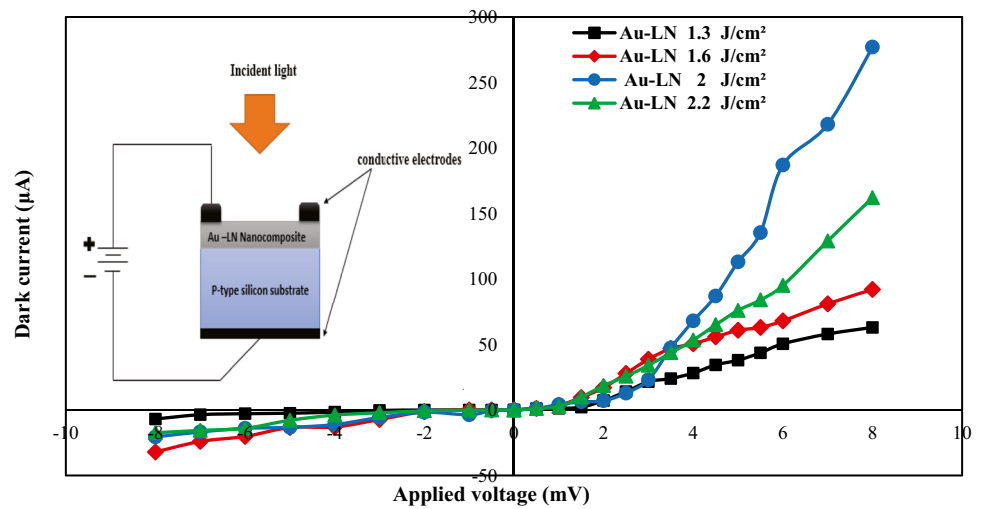
of Au nanoparticles is critical in reducing e–h recombination caused by the induction of a high electric field region and increasing photocurrent of the photodetector [58, 59]. The external quantum efficiency EQE of the photodetector can be defined is the ratio of incident number of photons to number of generated electrons. It can be determined from the following relationship:

$$EQE = \frac{1240R_\lambda}{\lambda(nm)} \tag{5}$$

The value of EQE at 400 nm for the photodetectors prepared at laser fluences of 1.3, 1.6, 2, and 2.2 J/cm^2 was estimated from Eq. (5) and found to be 0.33, 0.48, 1.3, and 1.13, respectively, at a bias voltage of -8 V. As shown, the value of EQE is larger than unity, which can be explained as follows: the width of the depletion region widens as the reverse bias voltage is applied, suggesting that the device is fully depleted at this voltage, resulting in efficient photogenerated carrier collection [60]. Furthermore, the applied bias voltage improves charge

injections and forms free carriers, which absorb light photons and increase quantum efficiency dramatically through the photomultiplication effect. The figures of merit of the fabricated photodetector have been compared with other heterojunction-based silicon photodetectors as depicted in Table 3.

An energy band diagram has been constructed to understand the rectifying properties of the fabricated device, as shown in Fig. 19. The electron affinity of silicon is 4.05 eV, and its energy gap is 1.1 eV at room temperature, and the work function of Au is 5 eV. Crystalline Au@LN deposited using the LAL method is usually Li ion deficient. Its band gap at optimum laser fluence is found to be 3.8 eV. LN's electron affinity is currently thought to be unaffected by impurity levels, with a value of 1.1 eV [65]. The band offsets of LN/Si heterojunction wee estimated and found to be $\Delta E_C = \chi_{Si} - \chi_{LN} = 4.05 - 1.1 = 2.95$ eV and $\Delta E_V = \chi_{Si} + Eg_{Si} - (\chi_{LN} + Eg_{LN}) = 4.05 + 1.12 - (1.1 + 3.8) = 0.27$ eV. It is noteworthy that the electron jumps from Au to LN to substitute for the missing electron via the recombination process.
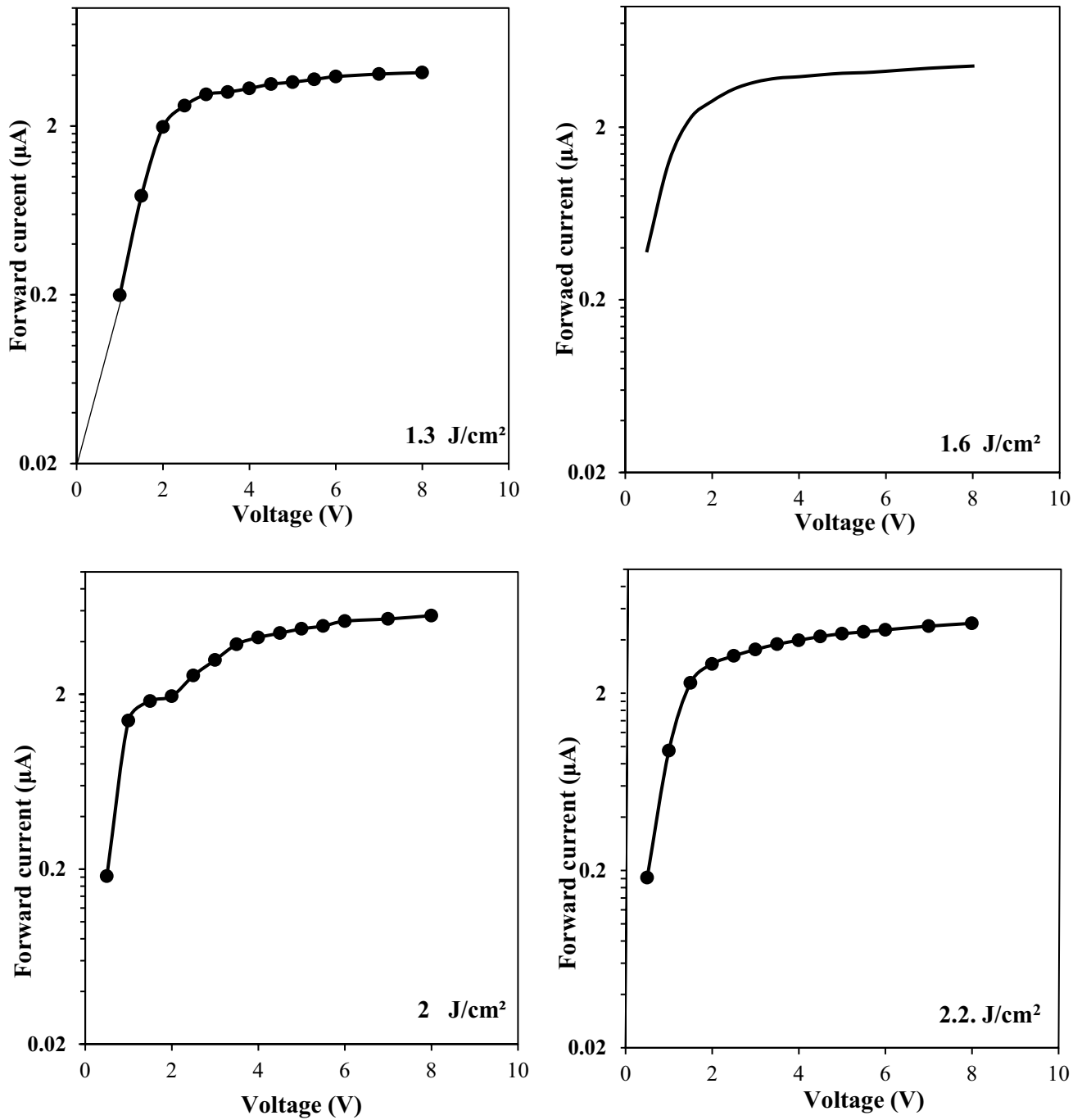
Fig. 14 Semi logarithmic relationship of forward current–voltage characteristics of heterojunctions prepared at different laser fluences

Fig. 15 **a** Variation of junction capacitance with reverse voltage and **b** $1/C^2$ versus voltage of p-Au@LiNbO$_3$/p-Si heterojunctions fabricated at different laser fluences
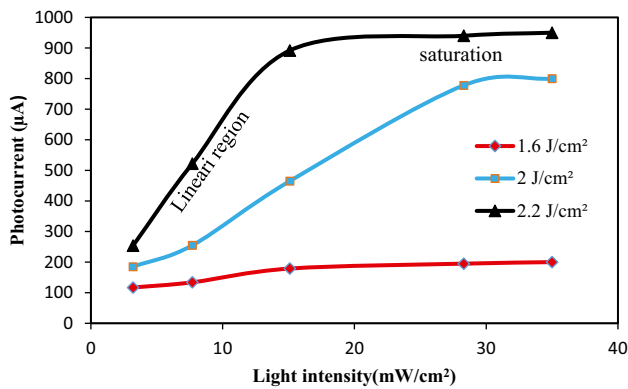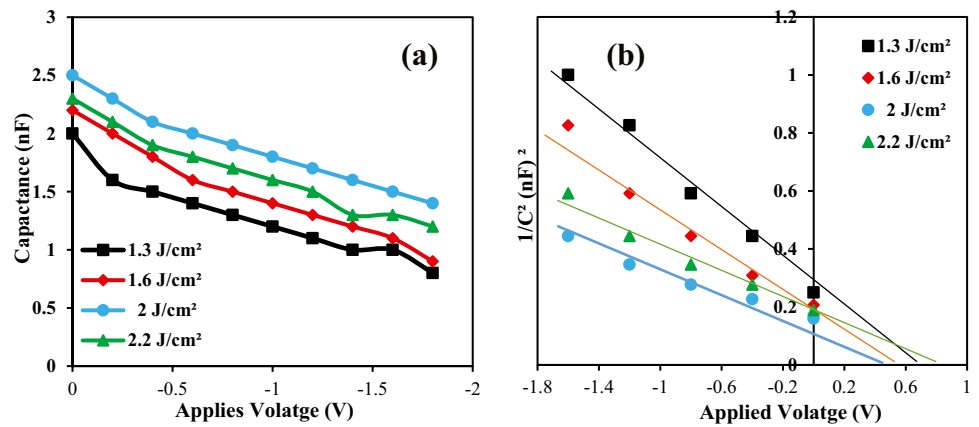

Fig. 16 Variation of photocurrent with light intensity of p-Au@LiNbO$_3$/p-Si heterojunctions fabricated at different laser fluences
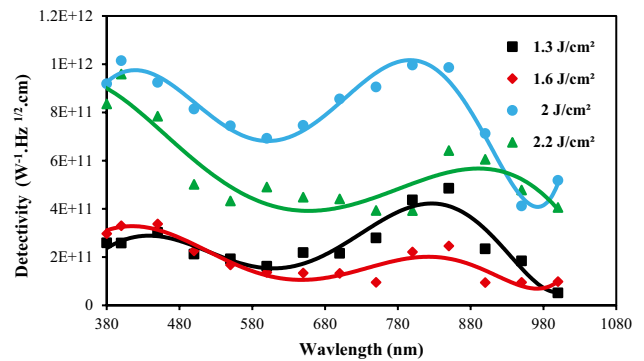
Fig. 18 Specific detectivity of p-Au@LiNbO$_3$/p-Si photodetectors at reverse bias voltage of − 8 V
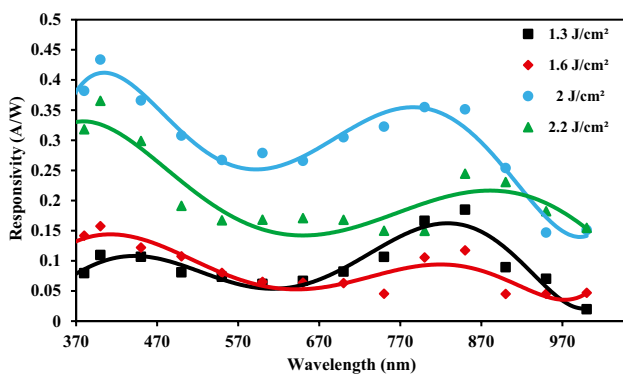
Fig. 17 Spectral responsivity of p-Au@LiNbO$_3$/p-Si photodetectors fabricated at different laser fluences at bias of 8 V

Table 3 A comparison of the figures of merit of the fabricated photodetector with those for other heterojunction-based silicon photodetectors

Photodetector	Responsivity (A/W)	Detectivity (Jones)	EQE %	LDR (dB)
Bi_2Te_3/Si [61]	0.97 at 635 nm	2.5×10^{11} at 635 nm	1.9×10^2 at 635 nm	-
CdTe/Si [62]	0.5 at 950 nm	1.2×10^{11} at 950 nm	65 at 950 nm	-
CuO@CuS/Si [63]	0.79 at 390 nm	8.11×10^{11} at 390 nm	3.09×10^2 at 390 nm	-
$Au@PbI_2$/Si [64]	0.39 at 800 nm	4×10^{12} at 800 nm	60.4 at 800	-
This work	0.43 at 400 nm	1.01×10^{12} at 400 nm	1.3×10^2 at 400 nm	152

Fig. 19 Energy band diagram of $Au@LiNbO_3$/p-Si photodetector prepared at 2.2 J/cm^2
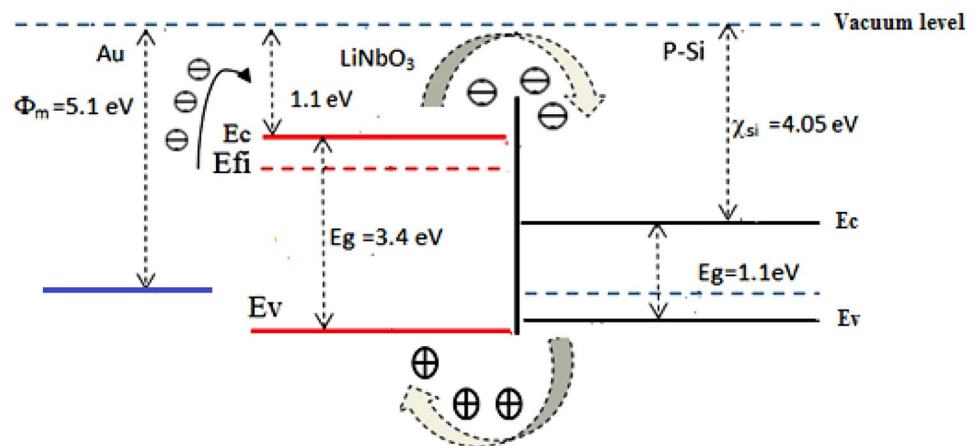
Conclusion

We have successfully synthesized an $Au@LiNbO_3$ core/shell structure using pulsed laser ablation in ethanol without using catalyst. The variation of laser fluence affects the structural, optical, and electrical properties of $Au@LiNbO_3$ core/shell. The presence of peaks related to $LiNbO_3$ and Au in the XRD data revealed that the product has a polycrystalline structure and confirmed the formation of the core/shell structure. The TEM investigation confirmed the formation of core/shell nanoparticles with a spherical shape, with the gold core surrounded by a $LiNbO_3$ shell. The laser fluence was found to increase shell thickness. The current–voltage properties of $Au@LiNbO_3$/Si confirmed the formation of a good heterojunction with a rectification factor that depends on the laser fluence. The parameters of an isotype $Au@LiNbO_3$/Si heterojunction photodetector as a function of laser fluence were investigated. The spectral responsivity results revealed that the fabricated photodetectors have two peaks of response, specifically located at 399 and 50 nm. The maximum responsivity was 0.43A/W at 399 nm for the photodetector fabricated with a laser fluence of 2 J/cm^2. Increasing the responsivity in the visible region through the insertion of a buffer layer and

selection the optimum preparation conditions is underway. The findings of this work confirm that the characteristics of core/shell synthesized in an ethanol medium are better than those obtained in distilled water due to the lower particle agglomeration.

Data Availability No applicable.

Declarations

Conflict of Interest The authors declare no competing interests.

References

1. Rüter CE, Brüske D, Suntsov S, Kip D (2020) Investigation of ytterbium incorporation in lithium niobate for active waveguide devices. Appl Sci 10:2189

2. Huang J, Zhang D, Qi Z, Zhang B, Wang H (2021) Hybrid Ag–LiNbO3 nanocomposite thin films with tailorable optical properties. Nanoscale Adv 3:1121–1126

3. Meriche F et al (2010) Fabrication and investigation of 1D and 2D structures in LiNbO3 thin films by pulsed laser ablation. Opt Mater (Amst) 32:1427–1434

4. Fakhri MA, AbdulRazzaq MJ, Alwahib AA, Muttlak WH (2020) Theoretical study of a pure LinbO3/Quartz waveguide coated gold nanorods using supercontinuum laser source. Opt Mater 109:110363

5. Jeong IK, Park S (2011) Correlated thermal motion in ferroelectric LiNbO3 studied using neutron total scattering and a rietveld analysis. J Korean Phys Soc 59:2756–2759

6. Taleb SM, Fakhri MA, Adnanm SA (2020) Optical Investigations of Nanophotonic LiNbO3 Films Deposited by Pulsed Laser Deposition Method, Defect and Diffusion. Forum 398:16–22

7. Meriche F et al (2007) Micro structuring of LiNbO3 by using nanosecond pulsed laser ablation. Appl Surf Sci 254:1327–1331

8. Taleb SM, Fakhri MA, Adnan SA (2019) Physical investigations of nanophotonic LiNbO3 films for photonic applications. J Ovonic Res 15(4):261–269

9. Lee SH, Noh TW (1998) Nonlinear optical properties of LiNbO3/Al2O3 films epitaxially grown by pulsed laser deposition. Integr Ferroelectr 20:25–37

10. Balestrino G et al (2001) Epitaxial LiNbO3 thin films grown by pulsed laser deposition for optical waveguides. Appl Phys Lett 78:1204–1206

11. Fakhri MA, Al-Douri Y, Bouhemadou A, Ameri M (2017) Structural and optical properties of nanophotonic LiNbO 3 under stirrer time effect. J Opt Commun 39(3):297–306

12. Qi Y, Li Y (2020) Integrated lithium niobate photonics. Nanophotonics 9:1287–1320

13. Desiatov B, Lončar M (2019) Silicon photodetector for integrated lithium niobate photonics. Appl Phys Lett 115:12

14. Al-Douri Y, Fakhri MA, Badi N, Voon CH (2018) Effect of stirring time on the structural parameters of nanophotonic LiNbO3 deposited by spin-coating technique. Optik 156:886–890

15. Wang X, Ye Z, He J, Cao L, Zhao B (2004) The role of SiO2 buffer layer in the growth of highly textured LiNbO3 thin film upon SiO2/Si by pulsed laser deposition. Mater Lett 58(200):3597–3600

16. Fakhri MA, Al-Douri Y, Hashim U, Salim ET, Prakash D, Verma KD (2015) Optical investigation of nanophotonic lithium niobate-based optical waveguide. Appl Phys B: Lasers Opt 121(1):107–116

17. Kakehi Y, Okamoto A, Sakurai Y, Nishikawa Y, Yotsuya T, Ogawa S (2001) Epitaxial growth of LiNbO3 thin films using pulsed laser deposition. Appl Surf Sci 169–170:560–563

18. Fakhri MA, Al-Douri Y, Salim ET, Hashim U, Yusof Y, Choo EB, Salim ZT, Jurn YN (2016) Structural properties and surface morphology analysis of nanophotonic LINBO3. ARPN J Eng Appl Sci 11(8):4974–4978

19. Taylor P, Klose F, Wöhlecke M, Kapphan S (1989) (Uv-excited luminescence of LiNbO3 and LiNbO3 : Mg. Ferroelectrics 92:181–187

20. Tumuluri A, Raju KCJ (2014) Luminescence of LiNbO3 polycrystalline ceramics: effect of Sc2O3 and Lu2O3 doping. Ceram Int 40:3371–3377

21. Shih WC, Wang TL, Sun XY, Wu MS (2008) Growth of c-axis-oriented LiNbO3 films on ZnO/SiO2/Si substrate by pulsed laser

22. Fakhri MA, Hashim U, Salim ET, Salim ZT (2016) Preparation and charactrization of photonic LiNbO3generated from mixing of new raw materials using spry pyrolysis method. J Mater Sci: Mater Electron 27(12):13105–13112

23. Li W et al (2019) Fabrication and characteristics of heavily Fe-doped LiNbO3/Si heterojunction. Materials (Basel) 12:1–7

24. Zhang J, Li Li, Xiao Z, Liu Di, Wang S, Zhang J, Hao Y, Zhang W (2016) Hollow sphere TiO2–ZrO2 prepared by self-assembly with polystyrene colloidal template for both photocatalytic degradation and H2 evolution from water splitting. ACS Sustain Chem Eng 4:2037–2046

25. Zhang M, Ngo TH, Rabiah NI, Otanicar TP, Phelan PE, Swaminathan R, Dai LL (2014) Core–shell and asymmetric polystyrene–gold composite particles via one-step pickering emulsion polymerization. Langmuir 30(201):75–82

26. Wang DP, Zeng HC (2009) Multifunctional roles of TiO2 nanoparticles for architecture of complex core−shells and hollow spheres of SiO2−TiO2−polyaniline system. Chem Mater 21:4811–4823

27. Mei Y, Lu Y, Polzer F, Ballauff M, Drechsler M (2007) Catalytic activity of palladium nanoparticles encapsulated in spherical polyelectrolyte brushes and core−shell microgels. Chem Mater 19:1062–1069

28. Salim ZT, Hashim U, Arshad MM, Fakhri MA, Salim ET (2017) Zinc oxide flakes-corolla lobes like nano combined structure for SAW applications. Mater Res Bull 86:215–219

29. Richter J et al (2014) Core-shell potassium niobate nanowires for enhanced nonlinear optical effects. Nanoscale 6:5200–5207

30. Nichols WT, Sasaki T, Koshizaki N (2006) Laser ablation of a platinum target in water. I. Ablation Mechanisms. J Appl Phys 100:114911

31. Fakhri MA, Salim ET, Hashim U, Abdulwahhab AW, Salim ZT (2017) Annealing temperature effect on structural and morphological properties of nano photonic LiNbO3. J Mater Sci: Mater Electron 28(22):16728–16735

32. Ismail RA, Mousa AM, Amin MH (2018) Synthesis of hybrid Au@PbI2 core-shell nanoparticles by pulsed laser ablation in ethanol. Mater Res Express 29:1–16

33. Khalil I, Chou CM, Tsai KL, Hsu S, Yehye WA, Hsiao VKS (2019) Gold nanofilm-coated porous silicon as surface-enhanced Raman Scattering substrate. Appl Sci 9:1–12

34. Fakhri MA, Wahid MH, Badr BA, Kadhim SM, Salim ET, Hashim U, Salim ZT (2007) Enhancement of Lithium Niobate nanophotonic structures via spin-coating technique for optical waveguides application. Eur Phys J 162(7):01004

35. Son JW, Orlov SS, Phillips B, Hesselink L (2006) Pulsed laser deposition of single phase LiNbO3 thin film waveguides. J Electroceramics 17:591–595

36. Fakhri MA, Wahid MH, Kadhim SM, Badr BA, Salim ET, Hashim U, Salim ZT (2017) The structure and optical properties of lithium niobate grown on quartz for photonics application. Eur Phys J Conf 162:01005

37. Sun D, Zhang G, Huang J, Wang H, Li Q (2014) Plant-mediated fabrication and surface enhanced raman property of flower-like Au@Pd nanoparticles. Materials (Basel) 7:1360–1369

38. Adnan SA, Tawfiq ZH, Fakhri MA (2020) Gold Nanoparticles in Liquid Based on Photonic Crystal Fiber PCF for Sensors Application Defect Diffus Forum 398:23–28

39. Chen Y, Yeh C (2002) Laser ablation method : Use of surfactants to form the dispersed Ag nanoparticles. Colloids Surf A: Physicochem Eng Asp 197:133–139

deposition for surface acoustic wave applications. Jpn J Appl Phys 47:4056–4405

40. Ali HS, Fakhri MA (2020) An overview of Au & photonic crystal fiber of sensors. Mater Sci Forum 1002:282–289

41. Ismail RA, Habubi NF, Abbod MM (2016) Preparation of high-sensitivity In₂S₃/Si heterojunction photodetector by chemical spray pyrolysis. Opt Quant Electron 48:455. https://doi.org/10.1007/s11082-016-0725-5

42. Kobayashi Y et al (2017) "Light scattering from polar and pseudoscalar modes in doped LiNbO3 and LiTaO₃ monocrystals humidity dependence of surface resistances of LiNbO3 and LiTaO3 single crystals. J Phys Conf Ser 918:012017

43. Jawad M, Ismail R, Yahea K (2011) Preparation of nanocrystalline Cu₂O thin film by pulsed laser deposition. Mater Sci: Mater Electron 22:1244–1247

44. Mohanty D, Chaubey GS, Yourdkhani A, Adireddy S, Caruntu G, Wiley JB (2012) Synthesis and piezoelectric response of cubic and spherical LiNbO 3 nanocrystals. RSC Adv 2:1913–1916

45. Fakhri MA, Salim ET, Wahid MH, Hashim U, Salim ZT (2018) Optical investigations and optical constant of nano lithium niobate deposited by spray pyrolysis technique with injection of Li2CO3 and Nb2O5 as raw materials. J Mater Sci: Mater Electron 29(11):9200–9208

46. Santulli AC, Zhou H, Berweger S, Raschke MB, Sutter E, Wong SS (2010) Synthesis of single-crystalline one-dimensional LiNbO3 nanowires. CrystEngComm 12:2675–2678

47. Fakhri MA, Salim ET, Abdulwahhab AW, Hashim U, Salim ZT (2018) Optical properties of micro and nano LiNbO3thin film prepared by spin coating. Opt Laser Technol 103:226–232

48. Shandilya S, Sharma A, Tomar M, Gupta V (2012) Optical properties of the c-axis oriented LiNbO₃ thin film. Thin Solid Films 520:2142–2146

49. Fakhri MA, Salim ET, Wahid MHA, Abdulwahhab AW, Salim ZT, Hashim U (2019) Heat treatment assisted-spin coating for LiNbO₃ films preparation: Their physical properties. J Phys Chem Solids 131:180–188

50. Zhu D et al (2009) The origin of the high diode-ideality factors in GaInN/GaN multiple quantum well light-emitting diodes. Appl Phys Lett 94:2–4

51. Mazari H, Benamara Z, Ameur K, Benseddik N, Bonnaud O, Olier R (2009) Influence of Ru 3 + ions at Al / GaAs interface on Schottky diodes. Int J Nanoelectron Mater 2:147–156

52. Ismail RA, Fadhil FA (2014) Effect of electric field on the properties of bismuth oxide nanoparticles prepared by laser ablation in water. J Mater Sci: Mater Electron 25:1435–1440. https://doi.org/10.1007/s10854-014-1747-z

53. Bengal W (2012) Schottky barrier of Al on chemically grown n-CdSe nanoparticles. Satyajit Saha a, Amit manna 22:77–83

54. Ismail RA (2009) Characteristics of P-Cu2O/N-Si heterojunction photodiode made by rapid thermal oxidation. J SemicondTechnology Sci 9:51–54

55. Macleod BA et al (2012) Built-in potential in conjugated polymer diodes with changing anode work function: interfacial states and deviation from the Schottky − Mott limit. J Phys Chem Lett 3:1202–1207

56. Ismail RA et al (2018) Preparation of low cost n-ZnO/MgO/p-Si heterojunction photodetector by laser ablation in liquid and spray pyrolysis. Materi Res Express 5.5:055018

57. Ismail RA, Hamoudi WK, Abbas HF (2018) Synthesis of Au nanoparticles–decorated CdS nanowires via laser ablation in liquid for optoelectronic applications. Appl Phys A 124:683

58. Mousa A, Ismail RA, Amin M (2019) Hybrid p-Au@PbI2/n-Si heterojunction photodetector prepared by pulsed laser ablation in liquid. Optik 183:933–941

59. Ismail RA, Abdul-Hamed RS (2017) Laser ablation of Au–CuO core–shell nanocomposite in water for optoelectronic devices. Mater Res Express 4:125020

60. Faisal AD, Ismail RA, Khalef WK et al (2020) Synthesis of ZnO nanorods on a silicon substrate via hydrothermal route for optoelectronic applications. Opt Quant Electron 52:212. https://doi.org/10.1007/s11082-020-02329-1

61. Yao J, Shao J, Wang Y, Zhao Z, Yang G (2015) Ultra-broadband and high response of the Bi2Te3–Si heterojunction and its application as a photodetector at room temperature in harsh working environments. Nanoscale 7:12535–12541

62. Ismai R, Hassan K, Abdulrazaq O, Abode H (2007) Optoelectronic properties of CdTe/Si heterojunction prepared by pulsed Nd:YAG-laser deposition technique. Mater Sci Semicond Process 10:19–23

63. Gunasekaran S, Thangaraju D, Marnadu R et al (2021) Photosensitive activity of fabricated core-shell composite nanostructured p-CuO@CuS/n-Si diode for photodetection applications. Sens Actuator A Phys 317:112373

64. Mousa AM, Ismail RA, Amin MH (2019) Hybrid p-Au@PbI₂/n-Si heterojunction photodetector prepared by pulsed laser ablation in liquid. Optik - Int J for Light Electron Opt 183:933–941

65. Li W, Cui J, Zheng D, Wang W, Wang S, Song S, Liu H, Kong Y, Xu J (2019) Fabrication and characteristics of heavily Fe-doped LiNbO₃/Si heterojunction. Materials 12:2659